Detection of anthropogenic dust using CALIPSO lidar measurements

Jianping Huang[1,*], Jingjing Liu[1,2], Bin Chen[1], Shaima L. Nasiri[3]

[1]Key Laboratory for Semi-Arid Climate Change of the Ministry of Education, College of Atmospheric Sciences, Lanzhou University, Lanzhou, 730000, China
[2]School of Mechanical and Instrument Engineering, Xi'an University of Technology, Xi'an 710048, China
[3]Department of Atmospheric Science, Texas A&M University, College Station, Texas

Submitted to ACP Special Issue
"Anthropogenic Dust and its Climate Impact"

[*]Corresponding author：hjp@lzu.edu.cn

Abstract

Anthropogenic dusts are those produced by human activities on disturbed soils, which are mainly cropland, pasture, and urbanized regions and are a subset of the total dust load which includes natural sources from desert regions. Our knowledge of anthropogenic dusts is still very limited due to a lack of data. To understand the contribution of anthropogenic dust to the total global dust load, it is important to identify them from total dust. In this study, a new technique for distinguishing anthropogenic dust from natural dust is proposed by using Cloud-Aerosol Lidar and Infrared Pathfinder Satellite Observation (CALIPSO) dust and planetary boundary layer (PBL) height retrievals along with a land use dataset. Using this technique, the global distribution of dust is analyzed and the relative contribution of anthropogenic and natural dust sources to regional and global emissions are estimated. Results reveal that local anthropogenic dust aerosol due to human activity, such as agriculture, industrial activity, transportation, and overgrazing, accounts for about 25% of the global continental dust load. Of these anthropogenic dust aerosols, more than 53% come from semi-arid and semi-wet regions. Annual mean anthropogenic dust column burden (DCB) values range from 0.42 g m^{-2} with a maximum in India to 0.12 g m^{-2} with a minimum in North America. A better understanding of anthropogenic dust emission will enable us to focus on human activities in these critical regions and with such knowledge we will be better able to improve global dust models and to explore the effects of anthropogenic emission on radiative forcing, climate change and air quality in the future.

1 Introduction

Dust accounts for some of the highest mass loadings in the atmosphere and plays an important role in modulating radiative forcing and climate via a number of complex processes (Huang et al., 2006a, 2006b, Su, et al., 2008, Huang et al., 2014). Although mineral dust is widely distributed and has a relatively large optical depth, the existing atmospheric dust load cannot be explained by natural sources alone (Tegen and Fung, 1995). The atmospheric dust load that originates from soils disturbed by human activities such as land use practices, which can be interpreted as "anthropogenic" dust (Tegen and Fung, 1995) can increase dust loading, which, in turn, affects the radiative forcing. It is critical to quantify the relative importance of different dust sources and the factors that affect dust emissions to understand the global dust cycle, including historical and future changes in dust emissions, as noted by Okin et al. (2011) and Bullard et al. (2011).

Anthropogenic dust primarily originates from agricultural practices (harvesting, ploughing, and overgrazing), changes in surface water (e.g., shrinking of the Caspian and Aral Seas and Owens Lake), and urban and industrial practices (e.g., construction, cement production, and transportation) (Prospero et al., 2002). Over the last few decades, more frequent warmer and dryer winters and springs in semi-arid and semi-wet regions (Huang et al., 2012), in concert with changes in vegetated land cover due to human activities, have likely increased anthropogenic dust emissions (Mahowald and Luo, 2003; Moulin and Chiapello, 2004; Tegen et al., 2004). Mulitza et al.(2010) demonstrated that the development of agriculture in the Sahel

3

67 corresponded to a large increase in dust emission and deposition in the region. The

68 current consensus is that up to half of the modern atmospheric dust load originates

69 from anthropogenically disturbed soils (Tegen et al., 2004). Sokolik and Toon (1996)

70 revealed that the direct solar radiative forcing from anthropogenic dust is very

71 uncertain; thus, forcing from anthropogenically generated dust aerosols may be

72 comparable to forcings from other anthropogenic aerosols. Therefore, a clear

73 understanding of anthropogenic dust emissions is critical for predicting how changes

74 in land use (and thus changes in land use policies) will influence dust emissions,

75 loading, and deposition in the future (Okin et al, 2011).

76   However, assessments of the role of anthropogenic activity in the atmospheric

77 dust cycle are limited by the accuracy of the available datasets (Mahowald et al.

78 2003a). There are large uncertainties regarding the impact of anthropogenic activities

79 on dust emissions (Sokolik and Toon, 1996). Understanding the radiative forcing

80 caused by dust both directly (e.g., by disturbing soils, removing vegetation cover, or

81 drying water bodies), and indirectly (e.g., by changing the climate or hydrological

82 cycle) requires an improved dataset. Although there are many examples of humans

83 altering their environment and thereby causing an additional dust burden, it is

84 challenging to separately quantify the natural and anthropogenic components of

85 mineral aerosols (Sagan et al., 1979). Sokolik and Toon (1996) made the rough

86 assumption that the dust production rate is linearly proportional to the dust source

87 area and estimated the amount of anthropogenic mineral aerosols through assessment

88 of the land area converted to desert by human activities. Tegen and Fung (1995)

89   estimated the anthropogenic contribution to mineral dust to be 30 to 50% of the total

90   dust burden in the atmosphere by using a three-dimensional atmospheric dust

91   transport model. Later, Tegen et al. (2004) provided an updated estimate by

92   comparing observations of visibility; they suggested that only 5 to 7% of mineral dust

93   is derived from anthropogenic sources by calibrating a dust-source model with

94   emission indices from dust storm observations. There is limited understanding of the

95   anthropogenic dust emissions because of the difficulty of identifying and measuring

96   them, which derives from strong heterogeneities in the sources (Mahowald et al.,

97   2003b). Ginoux et al. (2012) conducted one of the first studies that estimated

98   anthropogenic dust emissions using observations. They estimated that 25% of dust is

99   anthropogenic by using the Moderate Resolution Imaging Spectroradiometer (MODIS)

100   Deep Blue satellite products in combination with a land-use fraction dataset. A

101   limitation of these products is that they can be retrieved only over surfaces that are

102   bright at visible wavelengths, excluding forests and ocean surfaces. Additionally,

103   MODIS products do not include vertical distribution information and therefore cannot

104   readily exclude natural dust aerosols from deserts or marine seasalt aerosols that are

105   transported over anthropogenic sources.

106   The Cloud-Aerosol Lidar and Infrared Pathfinder Satellite Observations

107   (CALIPSO) satellite can actively remotely sense cloud and aerosol vertical profiles

108   (Winker et al., 2007, Hu et al., 2007a, 2007b, 2009, Chen et al. 2010). CALIPSO's

109   measurement of vertical resolution and polarization ratios can provide new insights

110   into global anthropogenic dust emissions. In this study, we develop a new technique

111   for detection of anthropogenic dust emissions that uses CALIPSO lidar measurements

112   and analyzes their global distribution. Section 2 presents the data used in this study,

113   and the method for separating anthropogenic from natural dust is outlined in Section 3.

114   Section 4 discusses the calculation of the anthropogenic dust column burden (DCB).

115   Section 5 presents the global distribution of anthropogenic dust. Finally, the

116   conclusions are presented in Section 6.

117   **2 Data**

118   **2.1 CALIPSO data**

119   This study relies on the CALIPSO Cloud-Aerosol Lidar with Orthogonal

120   Polarization (CALIOP) for dust detection. CALIOP acquires vertical profiles of

121   elastic backscatter at two wavelengths (532 and 1064 nm) and linear depolarization at

122   532 nm from a near nadir-viewing geometry during both day and night (Winker et al.,

123   2007, Hu et al., 2007a, 2007b, 2009, Chen et al., 2010). This study uses Level 1

124   backscatter, depolarization ratio, and color ratio profiles along with the Level 2

125   Vertical Feature Mask (VFM) products and 5-km Aerosol Profile Products. The

126   depolarization ratio is a useful indicator for identifying non-spherical particles, and it

127   can distinguish between atmospheric dust and spherical aerosols (Liu et al., 2004, Sun

128   et al., 2013). The CALIPSO algorithm classifies aerosol layers that have volume

129   depolarization ratio (δ_v) greater than 0.075 as dust (Omar et al., 2009; Mielonen et al.,

130   2009). Mielonen et al. (2009) also confirmed that classification of dust is more

131   reliable than classification of fine aerosols because depolarization ratio can be used to

132   distinguish non-spherical aerosols from spherical ones while the color ratio is

6

133   sensitive mainly to particle size.

134   The CALIPSO Level 2 lidar VFM product (Liu et al., 2004; Vaughan et al., 2004)

135   provides information about cloud and aerosol layer boundaries and positions. In

136   CALIPSO Version 3 VFM data, the cloud aerosol discrimination (CAD) algorithm

137   separates clouds and aerosols based on multi-dimensional histograms of scattering

138   properties (e.g., intensity and spectral dependence), that is, the altitude-and

139   latitude-dependent feature integrated color ratio, χ', the layer-integrated volume

140   depolarization ratio, δ_v, and the feature mean attenuated backscatter coefficient, β'_{532}

141   (Liu et al., 2010). A parameter (CAD score) indicates a confidence at which a feature

142   (aerosol or cloud) can be distinguished using the CAD algorithm. Liu et al. (2010)

143   revealed that the feature classification is more reasonable if a higher magnitude of the

144   absolute value of CAD score is used and suggested applying a CAD score larger than

145   70. In our study, we selected a features where the $|CAD| \geqslant 70$ as well.

146   The Level 2 Aerosol Profile Product (Young and Vaughan, 2009) provides

147   profiles of particle extinction coefficient and backscatter and additional profile

148   information. In addition, the CALIPSO extinction quality control (QC) flags were

149   also provided. Extinction QC=0 (the lidar ratio is unchanged during the extinction

150   retrieval) and QC=1 (if the retrieval is constrained) are chosen in this paper，which are

151   used to calculate optical depth by integrating extinction coefficients. Chen et al. (2013)

152   noted that the impact of the screening procedure in this specific case is negligible.

153   **2.2 Land cover data**

154   The Collection 5.1 MODIS global land cover type product (MCD12C1) from

155 2011 is used in this study to provide anthropogenic dust source types. The MCD12C1

156 product has 0.05^{o} spatial resolution, includes 17 different surface vegetation types,

157 and was developed by the International Geosphere-Biosphere Programme data (IGBP)

158 (Loveland and Belward, 1997; Friedl et al., 2010). It provides the dominant land

159 cover type as well as the sub-grid frequency distribution of land cover classes within

160 each $0.05^{°}$ cell. Because we are focusing on sources of anthropogenic dust in this

161 paper, we limit our study to three agricultural surface types: Croplands, Grasslands,

162 and Cropland Mosaics. Cropland Mosaics are lands with a mosaic of croplands less

163 than 60% of the landscape (Friedl et al., 2002). Because urban environments can also

164 be sources of anthropogenic dust, we get information about the extent of urban areas

165 from the Global Rural-Urban Mapping Project (GRUMP) v1 (Schneider et al., 2010)

166 dataset. In Figure 1, we summarize the geographical distribution of the anthropogenic

167 dust source types described above. The colors indicate the locations of the four

168 different anthropogenic dust source types: red represents urban areas, orange

169 represents grassland, yellow represents cropland, and green represents cropland

170 mosaics. The four black rectangles denote four regions that will be emphasized later:

171 Eastern China, India, North America, and Africa.

172 **2.3 Precipitation data**

173   Anthropogenic dust emissions depend on soil moisture content and therefore on

174 precipitation and climate state. In this study, we use precipitation as a proxy for

175 climate state. The University of East Anglia Climate Research Unit (CRU) Global

176 Climate Dataset provides the monthly mean precipitation climatologies for global

177 land areas, excluding Antarctica (New et al., 1999), which is used in this study. The

178 data set is based on analysis of over 4000 individual weather station records and is

179 provided at 0.5 ° latitude and longitude resolution. The CRU Global Climate Dataset

180 temperature and precipitation, estimates were made for 80-100% of the land surface

181 (Mitchell and Jones, 2005). In this study the monthly mean climatology was

182 calculated relative to the average for the period 1961-1990.

183 **3 Calculation of dust column burden (DCB)**

184   Based on the detection methods described above, we are able to identify

185 anthropogenic dust and calculate anthropogenic dust column burden as a subset of the

186 global dust column burden. First, we used the dust extinction coefficient through the

187 parameter "Atmospheric Volume Description" which is used to discriminate between

188 aerosols and clouds in the CALIPSO Level 2 aerosol extinction profile products. Then,

189 dust extinction coefficients with higher confidence levels ($|CAD| \geqslant 70$) (Liu et al.,

190 2010) and quality-control (QC=0 or QC=1) based on the study of Chen et al. (2013)

191 were selected. Therefore, dust optical depth (DOD, τ) can be calculated by integrating

192 the CAD and QC quality-controlled extinction coefficient of dust aerosol over the

193 height of the dust layer.

194   After calculating global total DOD (τ_t) and anthropogenic DOD (τ_a) from the

195 CALIPSO profile products between January 2007 and December 2010, we were able

196 to calculate dust column burdens. The conversion from dust optical depth (τ) to dust

197 column mass burden (*M*) was calculated following Ginoux et al. (2001):

198
$$M = \frac{4}{3} \frac{r\, r_{eff}}{Q_{ext}} t = \frac{1}{e} t \quad (1)$$

9

199   Where, r_{eff} is the dust effective radius, ρ is the density of dust, Q_{ext} is the dust

200   extinction efficiency, and ε is the mass extinction efficiency. Ginoux et al. (2012) used

201   daily global DOD from MODIS deep blue aerosol products and converted it into

202   column burden. In this study, we follow those empirical values taken by Ginoux et al.

203   (2012) and assume r_{eff} = 1.2 μm, ρ =2600 kg m^{-3}, Q_{ext} = 2.5, ε = 0.6m^2 g^{-1}, and τ is

204   the dust optical depth derived from the CALIPSO retrievals.

205   **4 Dust Detection and Identification Methods**

206   It is a challenge to distinguish the anthropogenic dust component from natural

207   dust (Sagan et al., 1979; Sokolik and Toon, 1996) due to the indirect nature of the

208   satellite-based measurement data. In 2012, Ginoux et al. proposed a method to detect

209   anthropogenic dust by using MODIS deep blue products, but MODIS, a passive

210   instrument, has limited accuracy over relatively bright, land surfaces. In order to get

211   more accuracy and comprehensive results, we developed a new method to separate

212   natural and anthropogenic dust and assess anthropogenic impacts on dust emissions at

213   the global scale by using CALIPSO measurements.

214   Figure 2 shows a schematic of dust sources and vertical and horizontal transport

215   processes underlying our approach for separating anthropogenic dust from natural

216   dust. The yellow dots represent dust aerosol in the atmosphere; the arrows and red

217   wavy lines indicate lifting and turbulence, respectively. It illustrates that natural dust

218   from deserts can undergo long-range transport to other regions by lifting through the

219   planetary boundary layer (PBL) to the free troposphere, as confirmed by Chen et al.

220   (2013). Horizontal transport of natural dust aerosols occurs mainly above the PBL

221 (Jordan et al., 2010; Yu et al., 2012). Only a small amount of this dust enters and

222 remains within the PBL. However, it is this fraction that may be most relevant to air

223 quality (Yu et al., 2012). Dusts from other land surface types and pollution sources are

224 predominately trapped in the PBL where industrial and commercial activities, except

225 for air travel, are conducted (Stull, 1988; 2000). We go through four steps to

226 discriminate anthropogenic dust from natural dust in the CALIPSO data. The first step

227 is to detect the total dust load (both natural and anthropogenic).The second step is to

228 determine the source region of the dust. The third step is to determine the height of

229 PBL, and the final step is to determine which dust is anthropogenic dust i.e., that

230 subset of the total dust within PBL.

231 **4.1 Step 1: Total dust detection**

232 Aerosol subtypes are stored in the parameter "Feature Classification Flags" of

233 CALIPSO VFM data. Therefore, dust aerosols are identified by Feature Classification

234 Flags in this paper. We only use dust aerosol feature for which there is high

235 confidence, i.e., absolute values of CAD score greater than 70. Then, dust aerosol

236 extinction coefficients are integrated under the condition of extinctions QC=0 and

237 QC=1, which are chosen from CALIPSO's aerosol profile product. Next, we

238 calculated dust aerosol optical depth as well as dust column burden (g m^{-2}) in Eq. (1).

239 **4.2 Step 2: Selection of source regions of anthropogenic dust**

240 As stated previously, anthropogenic dust mainly comes from harvesting,

241 ploughing, overgrazing, construction, traffic, etc. We assume that anthropogenic dust

242 will typically be emitted from cropland, grasslands, and urban surfaces (referred to as

11

243   "anthropogenic surface"), will have thinner dust aerosol layers, will be predominately

244   trapped in PBL, and will rarely be lifted into the free atmosphere by wind and

245   turbulence. Therefore, we restrict our source regions to the urban, grassland, cropland,

246   and mosaic cropland surfaces from the MODIS and GRUMP datasets, as seen in Fig. 1.

247   **4.3 Step 3: Determination of PBL height**

248   In this step, we determine and use PBL height to exclude long-distance transport

249   of dust aerosol from dust sources above the anthropogenic surface described above, so

250   it is important to accurately determine PBL height to separate out the anthropogenic

251   dust.

252   We can use CALIPSO to determine PBL height because, in general, the PBL is

253   capped by a temperature inversion that tends to trap moisture and aerosols. The

254   gradient of backscatter seen by lidar is almost always associated with this temperature

255   inversion and the simultaneous decrease in moisture content (Palm et al., 1998; Melfi

256   et al., 1985). Thus, the definition of the PBL top as the location of the maximum

257   aerosol scattering gradient is analogous to the more conventional thermodynamic

258   definition. McGrath-Spangler and Denning (2012) revealed that the Modern-era

259   Retrospective Analysis for Research and Applications (MERRA) PBL depths are

260   within 25% of the estimates derived from the maximum standard technique (Jordan et

261   al., 2010) by CALIPSO, which is better than radiosonde estimates of space/time

262   average PBL depth (Angevine et al., 1994).

263   We modified the maximum standard technique developed by Jordan et al. (2010)

264   and derived global PBL heights using this method, which are consistent with results

of McGrath-Spangler and Denning (2012). And, we found that this technique compared favorably to the ground-based lidar at the Semi-Arid Climate and Environment Observatory of Lanzhou University (SACOL) (Huang et al., 2008) with a correlation coefficient of 0.73 (Liu et al., 2014).

4.4 Step 4: identification of anthropogenic dust within PBL

The final step is to identify the anthropogenic dust within the PBL. Two parameters, the layer integrated depolarization ratio δ' and the layer integrated attenuated backscatter coefficient γ', can be used to explore the difference in optical properties between natural dust and anthropogenic dust. As an illustration of the process and resulting output of this step, we chose two typical areas based on dust optical depth (τ), population density, and land cover distribution, to represent sources of anthropogenic dust (North China: 35.0-39.0 °N, 114.0-118.0 °E) and natural dust source (Taklamakan: 38.0-40.0 °N，78.0-83.0 °E). Because spring (March to May) is the most active season for dust emission in the Taklamakan region, 4 years (2007 through 2010) of spring, daytime CALIPSO measurements were used to look at the optical properties of natural dust aerosol. Because anthropogenic dust has little seasonal dependence and natural dust is at its minimum during autumn in Northern China.we used 4 years (2007 through 2010) of autumn measurements to look at the optical properties of anthropogenic dust. For these two seasons, the statistical distribution of the layer-integrated δ' and γ' for both anthropogenic dust and natural dust from the entire profile and within the PBL, respectively was constructed by summing occurrences within grid boxes of $\Delta\delta' - \Delta\gamma'$ measuring 0.01-by-0.001 sr^{-1}.

287   In Fig. 3 (a), we can see that a threshold of $\delta' = 0.25$ can be used to discriminate

288   dust based on the set of entire height profiles from the Taklamakan and North China.

289   Fig. 3 (b) shows that a lower threshold of $\delta' = 0.23$ can be used to separate

290   anthropogenic dust from natural dust within the PBL. The larger threshold value for

291   the entire profile compared to the PBL is mainly due to the fact that natural dust

292   transport above the PBL in North China leads to a larger depolarization ratio.

293   Furthermore, anthropogenic dust has lower layer-integrated attenuated backscatter

294   because anthropogenic dust produced by human activities is generally mixed with

295   other more spherical aerosol types within the PBL, which has lower non-spherical.

296   Natural dust is more non-spherical than anthropogenic dust, so anthropogenic dust has

297   lower layer-integrated depolarization ratio than natural dust.

298   Therefore, anthropogenic dust could be accurately distinguished from natural

299   dust by the above steps. Inevitably, there are some misclassifications of anthropogenic

300   and natural dust owing to anthropogenic dust mixed with natural dust above and

301   below the PBL. This problem should be kept in mind in the following results and

302   discussion. Quantitatively, ~ 9.6% of anthropogenic dust is misclassified as natural

303   dust and 8.7% of natural dust is misclassified as anthropogenic dust within the PBL

304   along with the anthropogenic dust, respectively.

305   A detailed flow chart of the anthropogenic dust detection algorithm is shown in

306   Figure 4.

307   **5 Results**

308   The global distributions of seasonal mean and total DOD with $1.25\,° \times 1.25\,°$

309   resolution derived from CALIPSO measurements for 2007-2010 are presented in Fig.

310   5. Dust covers a larger area in the Northern Hemisphere than in the Southern

311   Hemisphere. The Taklamakan and Gobi Deserts in China (Qian et al., 2002, Huang et

312   al., 2007, 2008) and the deserts on the Indian Subcontinent (Middleton, 1986) are

313   major dust source regions that are subordinate only to North Africa and the Arabian

314   Peninsula (Prospero et al., 2002; Liu et al., 2008). These major dust sources are

315   located in the broad "dust belt" that stretches from the western coast of North Africa

316   to China, covering the Sahara and Sahel regions, the Arabian Peninsula, northern

317   India, the Tarim Basin and the Gobi Desert (Herman et al., 1997; Prospero et al., 2002;

318   Liu et al., 2008, Huang et al., 2010, 2014). The dust sources are usually associated

319   with topographical basins in these arid regions, on land adjacent to high mountainous

320   or plateau regions or in intermountain basins as discussed in detail by Prospero et al.

321   (2002). The annual rainfall in these dust source regions is generally low, less than

322   200–250 mm. Significant seasonal variation in the DOD is illustrated panels (a)

323   through (d) of Fig. 5. Dust outbreaks are most active in this dust belt during the spring

324   and summer. In North Africa and the Arabian Peninsula, summer is the most active

325   season, where as spring is the most active season in the Indian subcontinent and the

326   Taklamakan region. In the Arabian Peninsula, the Indian subcontinent and

327   Taklamakan, dust activities weakens rapidly in autumn, reaching a minimum in winter.

328   Fig. 5 illustrates a major dust transport pathway, in which the trans-Atlantic transport

329   of North African dust stretches the "dust belt" towards the North American continent.

330   North African dust is transported across the Atlantic throughout the year, although

331   spring and summer are the most active seasons and autumn is the least active. Fig. 5

332   also shows that the Hexi Corridor is a transport pathway in East Asia, although it is

333   clearly subordinate to the North Atlantic pathway.

334   Using eq. (1), we calculated the global annual mean total DCB to be 79.3 Tg.

335   The global seasonal mean values, which are 81.5 (spring), 81.0 (summer), 73.7

336   (autumn) and 77.5 (winter) Tg, indicate that the dust burden in the atmosphere is

337   greater during the spring and summer. According to Huneeus et al. (2011), the global

338   annual mean dust burden values from 14 models range from 6.8 to 29.5 Tg. These

339   values are far less than our results, possibly because we include air masses with both

340   pollution aerosols and dust, thereby accounting for episodes in which dust mixes with

341   smoke from biomass burning, urban pollution and sea salt aerosols (Omar et al., 2009).

342   In these cases the depolarization ratio is dominated by the dust component, thus

343   causing the entire mixture to be classified as dust and imparting larger values to our

344   DCB values.

345   Fig. 6 illustrates the global distribution of the seasonal mean anthropogenic

346   DCBs. The global seasonal mean anthropogenic DCBs are 7.0 (spring), 6.9 (summer),

347   6.1 (autumn), and 6.0 (winter) Tg, respectively. This pattern differs from the seasonal

348   pattern of natural DOD (τ_n); the anthropogenic DCB has minimal seasonal variation

349   because anthropogenic dust emissions are controlled by human activities and urban

350   pollutants. Greater DCBs occurred in eastern China, India, and North Africa during all

351   seasons. These greater DCBs are related to higher population densities in eastern

352   China and India and biomass burning throughout the year in Africa when farmers are

353   preparing land for the agricultural season and grazing (Justice et al., 1996). The global

354   annual mean anthropogenic DCB is 6.7 Tg, which accounts for 8.4% of the total

355   global DCB. To avoid the impact of dust on the ocean, we only calculated global

356   continental dust aerosols. We found that anthropogenic dust sources account for

357   24.8% of total continental dust sources (including polluted dust). There are two

358   reasons for the difference between our results and those of Ginoux et al. (2012): first,

359   the MODIS Deep Blue algorithm only retrieves the DOD over bright surfaces

360   (excluding forest and oceans), thus leading to a lower dust burden. Second, MODIS

361   data products lack vertical information; therefore, they cannot extract natural dust

362   from deserts transported over anthropogenic sources regions, and thus they tend to

363   yield larger results.

364   Fig. 7 shows the global distribution of the anthropogenic dust percentage of the

365   total DCB over land. This figure illustrates the significance of human activities on

366   dust in many areas. Several features are evident in these maps. Highly populated or

367   intensively cultivated agricultural regions, such as eastern North America, India,

368   eastern China and Europe, all have anthropogenic dust percentages of greater than

369   60%. Lower percentages occur over places such as western North America,

370   particularly the Great Basin, and North Africa, where less human activity leads to

371   fewer anthropogenic dust aerosols.

372   Fig. 8 compares the global DCB as a function of climatological mean

373   precipitation for spring, summer, autumn, and winter. Although soil moisture is also

374   related to the surface temperature, the long-term mean precipitation is the simplest

375   index for classifying climate regions. The mean precipitation varies from less than

376   100 mm yr^{-1} to a maximum of 2000 mm yr^{-1} in Fig. 8, and the interval value is 100

377   mm yr^{-1}. The average anthropogenic DCB that corresponds to each precipitation

378   intervals is plotted. Fig. 8 shows that anthropogenic dust mainly comes from

379   semi-arid and semi-wet regions over the entire year. Semi-arid regions are transition

380   zones between arid and semi-wet regions. They are defined as areas in which the

381   precipitation is less than the potential evaporation, and are characterized by high

382   temperatures (30-45 ℃) during the hottest months. The annual mean precipitation

383   ranges from 200 to 600 mm yr^{-1} in semi-arid regions. Semi-wet regions cover

384   considerable parts of eastern North America, Europe, and central China, with

385   precipitation ranging from 600 to 800 mm yr^{-1}. The total anthropogenic DCB is

386   greater in spring and summer than in autumn and winter. This difference is most

387   significant in arid regions. There is almost no anthropogenic dust observed in arid

388   regions because of minimal agricultural and human activities and urban pollutions.

389   Table 1 presents the annual mean anthropogenic DOD (τ_a), total area, total

390   anthropogenic DCB and the percentage contribution to the total DCB from wet,

391   combined semi-arid and semi-wet, and arid regions. In wet regions the mean DOD is

392   0.12, and the anthropogenic contribution to the total DCB in wet regions is 80.3%.

393   This value is greater than the anthropogenic contributions from combined semi-arid

394   and semi-wet regions and arid regions, thus revealing that anthropogenic dust plays an

395   important role in determining the total amount of dust because the frequency of total

396   natural dust events (suspended dust, blowing dust, and dust storms) is lower in wet

18

397   regions. Table 1 suggests that anthropogenic dust aerosols from the combined

398   semi-arid and semi-wet regions contribute 52.5% to the total anthropogenic dust

399   aerosols over all three regions. The more frequent occurrence of anthropogenic dust

400   emissions over semi-wet and semi-arid regions may be related to greater human

401   activities and poor ecological practices in those regions.

402   Fig. 9 shows the regional distribution of the annual mean anthropogenic DCB

403   derived from CALIPSO measurements in four regions: Eastern China, India, North

404   America and North Africa. Table 2 lists their latitude and longitude ranges, the area

405   and percentage of each region that is considered to contribute to anthropogenic dust

406   emissions and the annual mean anthropogenic DCB of the regions. In India,

407   anthropogenic dust sources are distributed relatively evenly over the region; the

408   anthropogenic dust source area is 70.2% of the total area that is characterized by

409   intense agricultural and human activities (Prasad et al., 2007). In North Africa, we

410   note in Figs. 9 and 10 that the southern Sahel dust sources are overwhelmingly

411   anthropogenic and are associated with aerosols from biomass burning. There is a clear

412   separation between natural dust sources in the Sahara and anthropogenic dust in the

413   southern Sahel. The area dominated by anthropogenic dust sources is only 21.5% of

414   the total area; i.e., most of the area is dominated by natural dust sources. Fig. 9 also

415   shows that anthropogenic dust sources in Eastern China are mostly confined to areas

416   in the North-Eastern China, the North China Plain, and Inner Mongolia. The largest

417   anthropogenic DCBs are located over the North China Plain. This result is consistent

418   with the conclusions of Wang et al. (2006), who found that dust storm frequency does

19

419   not exceed 8 days per year in northern China, even where there are high levels of

420   human activity. In Mongolia, there are dozens of small anthropogenic dust sources

421   associated with pasturelands or grasslands. In North America, most dust sources are

422   centered in two eastern areas, the Great Plains and Upper Mississippi Valley and also

423   in the Great Basin to the west of the continental divide. A major difference from the

424   results of Ginoux et al. (2012) is that on the east side of the divide, anthropogenic and

425   natural dust sources are intertwined, and on the west side of the divide, the sources are

426   predominantly natural rather than anthropogenic. The largest anthropogenic DCBs are

427   distributed over Southeastern of North America.

428   A histogram that illustrates the relative contribution of anthropogenic and natural

429   dust sources over anthropogenic dust source surfaces for the four study regions is

430   shown in Fig. 10. The annual mean anthropogenic DCB values range from a

431   maximum of 0.42 g m^{-2} in India to a minimum of 0.12 g m^{-2} in North America,

432   including 0.23 g m^{-2} in eastern China and 0.24 g m^{-2} in North Africa. The

433   anthropogenic dust contributions to regional emissions from Eastern China and India

434   are 91.8% and 76.1%, respectively, followed by North America, with 73.9%. In recent

435   years, urbanization and human activities have increased in eastern China; thus, its

436   annual mean contribution of anthropogenic dust is the largest, approximately 91.8%.

437   In Africa, the Sahara Desert is a rich source of natural dust. Although the

438   anthropogenic dust contribution is minimal, it is greater than in North America and

439   eastern China. A lower amount of urban construction and human activity in North

440   America means that both its anthropogenic dust content and contribution are the

441 lowest of the four regions. A possible explanation for the above phenomenon is that

442 eastern China and India have larger population densities and thus more intense

443 agricultural and human activities.

6 Discussion and conclusions

445   Emission of soil and mineral dust particles from the Earth's surface is a

446 small-scale process that has global consequences (Okin et al., 2011), such as cloud

447 formation (Huang 2006b, 2010, 2014), anthropogenic carbon dioxide emission, snow

448 albedo changes (Huang et al., 2011), and land use changes (Sokolik et al., 2011). Dust

449 emissions are affected by climate variability and in turn can impact climate, air quality,

450 and human health (Ginoux et al., 2012). Global dust aerosols contain not only locally

451 emitted anthropogenic aerosols (including agricultural dust and industrial black

452 carbon) but also natural dust from deserts. Dust emissions from anthropogenic

453 activities could account for a large proportion of global dust emissions, but

454 quantifying anthropogenic dust emissions, is subject to large uncertainty (Sokolik and

455 Toon, 1996). In this paper, we have developed an algorithm to detect anthropogenic

456 dust based on CALIPSO measurements and the MODIS land cover dataset. Using this

457 algorithm, we determined the contribution of anthropogenic dust to the total global

458 dust load.

459   We conducted a case study to test our algorithm using CALIPSO data for the

460 Taklamakan Desert and northern China, both of which are known natural and

461 anthropogenic dust source regions respectively. We found that anthropogenic dust has

462 a layer-integrated depolarization ratio that is less than that of natural dust. This

463   difference exists because anthropogenic dust produced by human activities is

464   generally mixed with other types of aerosols within the PBL and is thus more

465   spherical than natural dust. However, we note that approximately 9.6% of

466   anthropogenic dust is misclassified as natural dust and 8.7% of natural dust is

467   misidentified as anthropogenic dust within the PBL. Another source of uncertainty in

468   the method comes from the uncertainty in the PBL depth and MODIS land cover.

469   Local anthropogenic dust aerosols from human activities such as agriculture and

470   industrial endeavors contribute 25% of the global continental dust load.

471   Anthropogenic dust aerosols mainly come from semi-arid and semi-wet regions,

472   which account for more than 52% of the total anthropogenic dust aerosols.

473   An analysis of sources over four different continental regions revealed regional

474   characteristics. The annual mean anthropogenic DCB value varies from 0.12 g m^{-2} in

475   North America to 0.42 g m^{-2} in India. Considering the mean DCB in the four regions,

476   the greatest burden of anthropogenic dust occurs over India, and the greatest burden

477   of natural dust occurs over Africa. On a percentage basis, anthropogenic dust is

478   greatest over eastern China, and natural dust is greater over Africa. Some studies have

479   confirmed that human activities (mainly farming, overgrazing, and water usage) are

480   likely responsible for the expansion of dust sources in northern China and India (Xuan

481   and Sokolik, 2002; Prasad et al., 2007). Igarashi et al. (2011) noted that drought has

482   been a contributing factor. Gong et al. (2004) demonstrated that although

483   desertification has increased by only a few percent in China, it has generated

484   disproportionately large areas of enhanced dust emissions. The relationship between

485   population density and the anthropogenic DCB from our four study regions further

486   supports the above results. As identified in this paper, anthropogenic dust mainly

487   comes from cropland, urban areas, and pasture. Anthropogenic dust from intermittent

488   dry lake basins is not considered. A major uncertainty in these results comes from the

489   assumption of a single value for the mass extinction efficiency in eq. (1) that was used

490   in this paper; this parameter probably varies among the different regions. To reduce

491   this uncertainty, it will be necessary to determine different mass extinction

492   efficiencies for natural and anthropogenic dust from different regions. We note that

493   the local anthropogenic dust also affects local climate, air quality, and human health.

494   Therefore, it is necessary to further investigate the interactions among

495   aerosol-cloud-precipitation processes and improve the parameterization of local air

496   pollution effects (Huang et al., 2006a, 2006b, 2010, 2014; Park et al., 2010; Li et al.,

497   2011).

498

499

507

508

509 **References**

510 Angevine, W. M., White, A. B., and Avery, S. K.: Boundary-layer depth and entrainment zone

511   characterization with a boundary-layer profiler, Boundary Layer Meteorol., 68, 375–385,

512   doi:10.1007/BF00706797, 1994.

513 Bullard, J. E., Harrison, S. P., Baddock, M., Drake, N. A., Gill, T. E., McTainsh, G. H., and Sun,

514   Y.: Preferential dust sources: A geomorphological classification designed for use in global

515   dust-cycle models, J. Geophys. Res., 116, F04034, doi:10.1029/2011JF002061, 2011.

516 Chen, B., J. Huang, P. Minnis, Y. Hu, Y. Yi, Z. Liu, D. Zhang, and X. Wang: Detection of dust

517   aerosol by combining CALIPSO active lidar and passive IIR measurements, Atmos. Chem.

518   Phys., 10, 4241-4251, doi:10.5194/acp-10-4241-2010, 2010.

519 Chen, S., Huang, J., Zhao, C., Qian, Y., Leung, L. R., and Yang B.: Modeling the transport and

520   radiative forcing of Taklamakan dust over the Tibetan Plateau: A case study in the summer of

521   2006,J. Geophys. Res., 118, 797–812, doi:10.1002/jgrd.50122, 2013.

522 Friedl, M. A., McIver, D. K., Hodges, J. C. F., Zhang, X. Y., Muchoney, D., Strahler, A. H.,

523   Woodcocka, C.E., Gopal, S., Schneider, A., Cooper, A., Baccini, A., Gao., F., and Schaaf, C.:

524   Global land cover mapping from MODIS: Algorithms and early results.RemoteSens. Environ.,

525   83, 287−302, 2002.

526 Friedl, M. A., Sulla-Menashe, D., Tan, B., Schneider, A., Ramankutty, N., Sibley, A., and Huang,

527   X.: MODIS Collection 5 global land cover: Algorithm refinements and characterization ofnew

528   datasets, RemoteSens. Environ., 114, 168-182,doi:10.1016/j.rse.2009.08.016, 2010.

529 Ginoux, P., Chin, M., Tegen, I., Prospero, J. M., Holben, B., Dubovik, O., and Lin, S. J.: Sources

530   and distributions of dust aerosols simulated with the GOCART model, J. Geophys. Res., 106,

531   20255-20273, doi:10.1029/2000JD000053, 2001.

532 Ginoux, P., Prospero, J. M., Gill, T. E., Hsu, N. C., and Zhao, M.: Global‐scale attribution of

533   anthropogenic and natural dust sources and their emission rates based on MODIS Deep Blue

534   aerosol products, Rev. Geophys., 50, RG3005, doi:10.1029/2012RG000388, 2012.

535 Gong, S., Zhang, X., Zhao, T., and Barrie, L.: Sensitivity of Asian dust storm to natural and

536   anthropogenic factors, Geophys. Res. Lett., 31, L07210, doi:10.1029/2004GL019502, 2004.

537 Hu, Y., Vaughan M., Liu Z., Lin, B., Yang. P., Flittner, D., Hunt, B., Kuehn, R., Huang, J., Wu,

538 D., Rodier, S., Powell, K., Trepte, C., and Winker D.: The depolarization - attenuated

539 backscatter relation: CALIPSO lidar measurements vs. theory, Optics Express, 15, 5327-5332,

540 2007a.

541 Hu, Y., Vaughan M., McClain, C., Behrenfeld, M., Sun-Mack, S., Flittner, D., Huang, J., Wielicki,

542 B., Minnis, P., Trepte, C., and Kuehn, R.: Global statistics of liquid water content and effective

543 number density of water clouds over ocean derived from combined CALIPSO and MODIS

544 measurements, Atmos. Chem. Phys., 7, 4065-4083, 2007b.

545 Hu, Y., Winker, D., Vaughan, M., Lin, B., Omar, A., Trepte, C., Flittner, D., Yang, P., Nasiri, S.

546 L., Baum, B., Sun, W., Liu, Z., Wang, Z., Young, S., Stamnes, K., Huang, J., Kuehn, R., and

547 Holz, R.: CALIPSO/CALIOP Cloud Phase Discrimination Algorithm, J. Atmos. Oceanic

548 Technol., 26, 2293-2309, 2009.

549 Herman, J., Bhartia, P., Torres, O., Hsu, C., Seftor, C., and Celarier, E.: Global distribution of UV

550 ‐ absorbing aerosols from Nimbus 7/TOMS data, J. Geophys. Res., 102,

551 16911-16922,doi:10.1029/96JD03680, 1997.

552 Huang, J., Minnis, P., Lin, B., Wang, T., Yi, Y., Hu, Y., Sun‐Mack, S., and Ayers, K.: Possible

553 influences of Asian dust aerosols on cloud properties and radiative forcing observed from

554 MODIS and CERES, Geophys. Res. Lett., 33, L06824, doi:10.1029/2005GL024724, 2006a.

555 Huang, J., Lin, B., Minnis, P., Wang, T., Wang, X., Hu, Y., Yi, Y., and Ayers, J. R.:

556 Satellite-based assessment of possible dust aerosols semi-direct effect on cloud water path over

557 East Asia,33, L19802, doi:10.1029/2006GL026561, 2006b.

558 Huang, J., J. Ge, and F. Weng: Detection of Asia dust storms using multisensor satellite

559 measurements, Remote Sens. Environ., 110, 186-191, 2007.

560 Huang, J., W. Zhang, J. Zuo, J. Bi, J. Shi, X. Wang, Z. Chang, Z. Huang, S. Yang, B. Zhang, G.

561 Wang, G. Feng, J. Yuan, L. Zhang, H. Zuo, S. Wang, C. Fu and J. Chou, An overview of the

562 semi-arid climate and environment research observatory over the Loess Plateau, Advances in

563 Atmospheric Sciences, 25, 906-921, doi:10.1007/s00376-008-0906-7, 2008.

564 Huang, J., Minnis, P., Yan, H., Yi, Y., Chen, B., Zhang, L., and Ayers, J.: Dust aerosol effect on

565 semi-arid climate over Northwest China detected from A-Train satellite measurements, Atmos.

566 Chem. Phys., 10, 6863-6872, doi:10.5194/acp-10-6863-2010, 2010.

567 Huang, J., Fu, Q., Zhang, W., Wang, X., Zhang, R., Ye, H., and Warren, S. G.: Dust and black

568   carbon in seasonal snow across northern China, Bull. Amer. Meteor. Soc.,92,

569   175–181,doi:10.1175/2010BAMS3064.1, 2011.

570   Huang, J., X. Guan, and F. Ji, Enhanced cold-season warming in semi-arid regions, Atmos. Chem.

571   Phys., 12, 5391-5398, doi:10.5194/acp-12-5391-2012, 2012.

572   Huang, J., Wang, T., Wang, W., Li, Z., and Yan, H.: Climate effects of dust aerosols over East

573   Asian arid and semi-arid regions, J. Geophys. Res., 119, 11,398–11,416,

574   doi:10.1002/2014JD021796, 2014.

575   Huang, Z., J. Huang, J. Bi, G. Wang, W. Wang, Q. Fu, Z. Li, S. Tsay, and J. Shi, Dust aerosol

576   vertical structure measurements using three MPL lidars during 2008 China-U.S. joint dust field

577   experiment, J. Geophys. Res., 115, D00K15, doi:10.1029/2009JD013273, 2010.

578   Huneeus, N., Schulz, M., Balkanski, Y., Griesfeller, J., Prospero, J., Kinne, S., Bauer, S., Boucher,

579   O., Chin, M., and Dentener, F.: Global dust model intercomparison in AeroCom phase I, Atmos.

580   Chem. Phys., 11, 7781-7816, doi:10.5194/acp-11-7781-2011, 2011.

581   Igarashi, Y., Fujiwara, H., and Jugder, D.: Change of the Asian dust source region deduced from

582   the composition of anthropogenic radionuclides in surface soil in Mongolia, Atmos. Chem.

583   Phys., 11, 7069-7080, doi:10.5194/acp-11-7069-2011, 2011.

584   Jordan, N. S., Hoff, R. M., and Bacmeister, J. T.: Validation of Goddard Earth Observing System

585   ‐ version 5 MERRA planetary boundary layer heights using CALIPSO, J. Geophys. Res., 115,

586   D24218, doi:10.1029/2009JD013777, 2010.

587   Justice, C., Kendall, J., Dowty, P., and Scholes, R.: Satellite remote sensing of fires during the

588   SAFARI campaign using NOAA advanced very high resolution radiometer data, J. Geophys.

589   Res., 101, 23851-23863, doi:10.1029/95JD00623, 1996.

590   Li Z., Li, C., Chen, H., Tsay, S.-C., Holben, B., Huang, J., Li, B., Maring, H., Qian, Y., Shi, G.,

591   Xia, X., Yin, Y., Zheng, Y., and Zhuang, G.: East Asian Studies of Tropospheric Aerosols and

592   their Impact on Regional Climate (EAST-AIRC): An overview,J. Geophys. Res., 116, D00K34,

593   doi:10.1029/2010JD015257, 2011.

594   Liu, D., Wang, Z., Liu, Z., Winker, D., and Trepte, C.: A height resolved global view of dust

595   aerosols from the first year CALIPSO lidar measurements, J. Geophys. Res., 113, D16214,

596   doi:10.1029/2007JD009776, 2008.

597   Liu, Z., Vaughan, M. A., Winker, D. M., Hostetler, C. A., Poole, L. R., Hlavka, D., Hart, W., and

598   McGill, M.: Use of probability distribution functions for discriminating between cloud and

599   aerosol in lidar backscatter data, J. Geophys. Res., 109, D15202, doi:10.1029/2004JD004732,

600   2004.

601   Liu, Z., Liu, D., Huang, J., Vaughan, M., Uno, I., Sugimoto, N., Kittaka, C., Trepte, C., Wang, Z.,

602   and Hostetler, C.: Airborne dust distributions over the Tibetan Plateau and surrounding areas

603   derived from the first year of CALIPSO lidar observations, Atmos. Chem. Phys., 8, 5045-5060,

604   doi:10.5194/acp-8-5045-2008, 2008.

605   Liu, Z., Kuehn, R., Vaughan, M., Winker, D., Omar, A., Powell, K., Trepte, C., Hu, Y., and

606   Hostetler, C.: The CALIPSO cloud and aerosol discrimination: Version 3 algorithm and test

607   results, 25th International Laser Radar Conference (ILRC), St. Petersburg, Russia, 5-9, 2010.

608   Liu, J., Huang, J., Chen, B., Zhou, T., Yan, H., Jin, H., Huang, Z., Zhang, B.: Comparisons of

609   PBL   heights   derived   from   CALIPSO   and   ECMWF   reanalysis   data   over   China,

610   doi:10.1016/j.jqsrt.2014.10.011, 2014.

611   Loveland, T. R., andBelward, A. S.: The IGBP-DIS global 1km landcover data set, DISCover:

612   First   results,   International   Journal   of   Remote   Sensing,   18,3289-3295,doi:

613   10.1080/014311697217099, 1997.

614   Mahowald, N. M., and Luo, C.: A less dusty future? Geophys. Res. Lett.,30, NO. 17, 1903,

615   doi:10.1029/2003GL017880, 2003.

616   Mahowald, N. M., Bryant, R. G., Corral, del J., and Steinberger, L.: Ephemeral lakes and desert

617   dust sources, Geophys. Res. Lett., 30, NO. 2, 1074, doi:10.1029/2002GL016041, 2003.

618   McGrath‑Spangler, E. L., and Denning, A. S.: Estimates of North American summertime

619   planetary boundary layer depths derived from space‑borne lidar, J. Geophys. Res., 117,

620   D15101, doi:10.1029/2012JD017615, 2012.

621   Melfi, S., Spinhirne, J., Chou, S., and Palm, S.: Lidar observations of vertically organized

622   convection in the planetary boundary layer over the ocean, J. Climate Appl. Meteor., 24,

623   806–821, 1985.

624   Mielonen, T., Arola, A., Komppula, M., Kukkonen, J., Koskinen, J., de Leeuw, G., and Lehtinen,

625   K.: Comparison of CALIOP level 2 aerosol subtypes to aerosol types derived from AERONET

626   inversion data, Geophys. Res. Lett., 36, L18804, doi:10.1029/2009GL039609, 2009.

627   Middleton, N.: A geography of dust storms in South‑West Asia, J. Climate., 6, 183-196,

628   doi:10.1002/joc.3370060207, 1986.

629   Mitchell, T. D., and Jones, P. D.: An improved method of constructing a database of monthly

630   climate observations and associated high-resolution grids, Int. J. Climatol., 25:

631   693–712,doi:10.1002/joc.1181, 2005.

632   Moulin, C., and Chiapello, I.: Evidence of the control of summer atmospheric transport of African

633   dust over the Atlantic by Sahel sources from TOMS satellites (1979–2000), Geophys. Res.

634   Lett.,31, L02107, doi:10.1029/2003GL018931, 2004.

635   Mulitza, S., Heslop, D., Pittauerova, D., Fischer, H. W., Meyer, I., Stuut, J.-B., Zabel, M.,

636   Mollenhauer, G., Collins, J. A., and Kuhnert, H.: Increase in African dust flux at the onset of

637   commercial agriculture in the Sahel region, Nature, 466, 226-228, doi:10.1038/nature09213

638   2010.

639   New, M., Hulme, M., and Jones, P.: Representing Twentieth-Century Space-Time Climate

640   Variability. Part I: Development of a 1961-90 Mean Monthly Terrestrial Climatology, J.

641   Climate, 12, 829–856, 1999.

642   Okin, G. S., Bullard, J. E., Reynolds, R. L., Ballantine, J. A. C., Schepanski, K., Todd, M. C.,

643   Belnap, J., Baddock, M. C., Gill, T. E., and Miller, M. E.: Dust: Small‐scale processes with

644   global consequences, Eos, Transactions American Geophysical Union, 92, 241-242,

645   doi:10.1029/2011EO290001, 2011.

646   Omar, A. H., Winker, D. M., Kittaka, C., Vaughan, M. A., Liu, Z., Hu, Y., Trepte, C. R., Rogers,

647   R. R., Ferrare, R. A., and Lee, K.-P.: The CALIPSO automated aerosol classification and lidar

648   ratio   selection   algorithm,   J.   Atmos.   Oceanic   Technol.,26,   1994–2014,

649   doi:10.1175/2009JTECHA1231.1, 2009.

650   Palm, S. P., Hagan, D., Schwemmer, G., and Melfi, S.: Inference of marine atmospheric boundary

651   layer moisture and temperature structure using airborne lidar and infrared radiometer data, J.

652   Appl. Meteor., 37, 308–324, doi:10.1175/1520-0450-37.3.308, 1998.

653   Park, S. H., S. L. Gong, W. Gong, P. A. Makar, M. D. Moran, J. Zhang, and C. A. Stroud:

654   Relative impact of windblown dust versus anthropogenic fugitive dust in PM2.5 on air quality

655   in North America, J. Geophys. Res., 115, D16210, doi:10.1029/2009JD013144, 2010.

656   Prasad, A. K., Singh, S., Chauhan, S., Srivastava, M. K., Singh, R. P., and Singh, R.: Aerosol

657   radiative forcing over the Indo-Gangetic plains during major dust storms, Atmos. Environ., 41,

658   6289-6301, doi:10.1016/j.atmosenv.2007.03.060, 2007.

659   Prospero, J. M., Ginoux, P., Torres, O., Nicholson, S. E., and Gill, T. E.: Environmental

660   characterization of global sources of atmospheric soil dust identified with the Nimbus 7 Total

661   Ozone Mapping Spectrometer (TOMS) absorbing aerosol product, Rev. Geophys., 40, 2-1-2-31,

662   doi:10.1029/2000RG000095, 2002.

663   Qian, W., Quan, L., and Shi, S.: Variations of the Dust Storm in China and its Climatic Control, J.

664   Climate, 15, 1216–1229, 2002.

665   Sagan, C., Toon, O. B., Pollack, J. B.: Anthropogenic Albedo Changes and the Earth's Climate,
666   Science, 206, 1363-1368, 1979.

667   Schneider, A., Friedl, M. A., and Potere, D.: Mapping global urban areas using MODIS 500-m

668   data: New methods and datasets based on 'urban ecoregions', Remote Sens. Environ., 114,

669   1733-1746, doi:10.1016/j.rse.2010.03.003, 2010.

670   Sokolik, I. N., and Toon, O. B.: Direct radiative forcing by anthropogenic airborne mineral

671   aerosols, Nature, 381, 681-683, 1996.

672   Sokolik, I. N., Curry, J., and Radionov, V.: Interactions of Arctic aerosols with land-cover and

673   land-use changes in Northern Eurasia and their role in the Arctic climate system, in: Eurasian

674   Arctic Land Cover and Land Use in a Changing Climate, Springer, 237-268,

675   doi:10.1007/978-90-481-9118-5_10, 2011.

676   Stull, R. B.: An Introduction to Boundary Layer Meteorology,666 pp. Kluwer Acad., Norwell,

677   Mass, 1988.

678   Stull, R. B.: Meteorology for Scientists and Engineers, Brooks/Cole,Pacific Grove, Calif., 2000.

679   Su, J., J. Huang, Q. Fu, P. Minnis, J. Ge, and J. Bi, Estimation of Asian dust aerosol effect on

680   cloud radiation forcing using Fu-Liouradiative model and CERES measurements, Atmos. Chem.

681   Phys., 8, 2763-2771, 2008.

682   Sun, W., Z. Liu, G. Videen, Q. Fu, K. Muinonen, D. Winker, C. Lukashin, Z. Jin, B. Lin, and J.

683   Huang, For the depolarization of linearly polarized light by smake particles, Journal of

684   Quantitative Spectroscopy & Radiative Transfer, 122, 233-237, 2013

685   Tegen, I., and Fung, I.: Contribution to the atmospheric mineral aerosol load from land surface

686   modification, J. Geophys. Res., 100, 18707-18726, doi:10.1029/95JD02051, 1995.

687   Tegen, I., Werner, M., Harrison, S., and Kohfeld, K.: Relative importance of climate and land use

688   in determining present and future global soil dust emission, Geophys. Res. Lett., 31, L05105,

689   doi:10.1029/2003GL019216, 2004.

690   Vaughan, M., Young, S., Winker, D., Powell, K., Omar, A., Liu,Z., Hu, Y., and Hostetler, C.:

691   Fully automated analysis of spacebased lidar data: an overview of the CALIPSO retrieval

692   algorithms and data products, Proc. SPIE Int. Soc. Opt. Eng., 5575,16–30, 2004.

693   Wang, X., Zhou, Z., and Dong, Z.: Control of dust emissions by geomorphic conditions, wind

694   environments and land use in northern China: An examination based on dust storm frequency

695   from 1960 to 2003, Geomorphology, 81, 292-308, doi:10.1016/j.geomorph.2006.04.015, 2006.

696   Winker, D. M., Hunt, W. H., and McGill, M. J.: Initial performance assessment of CALIOP,

697   Geophys. Res. Lett., 34, L19803, doi:10.1029/2007GL030135, 2007.

698   Xuan, J., and Sokolik, I. N.: Characterization of sources and emission rates of mineral dust in

699   Northern China, Atmos. Environ., 36, 4863-4876, doi:10.1016/S1352-2310(02)00585-X, 2002.

700   Young, S. A., and Vaughan, M. A.: The Retrieval of Profiles of Particulate Extinction from

701   Cloud-Aerosol Lidar Infrared Pathfinder Satellite Observations (CALIPSO) Data: Algorithm

702   Description. J. Atmos. Oceanic Technol.,26, 1105–1119, doi:10.1175/2008JTECHA1221.1,

703   2009.

704   Yu, H., Remer, L. A., Chin, M., Bian, H., Tan, Q., Yuan, T., and Zhang, Y.: Aerosols from

705   overseas   rival   domestic   emissions   over   North   America,   Science,   337,

706   566-569,doi:10.1126/science.1217576, 2012.

707

708 **Figure captions:**

709 Fig. 1. Global anthropogenic land cover (including urban, cropland and pasture)

710 distribution retrieved by combing MODIS and GRUMP data.

711 Fig. 2. A schematic figure for the detection process of anthropogenic dust.

712 Fig. 3. The relationship between the layer-integrated depolarization ratio and the

713 layer-integrated attenuated backscatter coefficient for anthropogenic dust (North

714 China) and natural dust (Taklamakan).

715 Fig. 4. Flow chart of anthropogenic dust detection by combing CALIPSO and land

716 cover dataset provided MODIS.

717 Fig. 5. Global seasonal distributions of total (including polluted dust) dust optical

718 depth derived from CALIPSO measurements (2007 - 2010).

719 Fig. 6. Global seasonal distributions of mean anthropogenic dust column burden
720 (2007- 2010). The gray areas represent non-anthropogenic dust source over land.

721 Fig. 7. Global distributions of the percentage of anthropogenic dust column burden

722 account for total dust column burden.

723 Fig. 8. Comparisons of dust column burden as function of climatological mean

724 precipitation for different four seasons (spring, summer, autumn, and winter) of global.

725 The precipitation interval is 100 mm yr^{-1}.

726 Fig. 9. Regional distribution of annual mean anthropogenic dust column burden

727 derived from CALIPSO measurements (2007 through 2010) for a) Eastern China, b)

728 India, c) North America, and d) North Africa.

729 Fig. 10. Anthropogenic (red) and natural (blue) mean dust column burdens and

730 percentages in four regions (Eastern China, India, North America and Africa).

731

732

733   Table 1. Summary of anthropogenic dust annual mean statistics by climate region.

734   Anthropogenic dust optical depth (ADOD); total regional area; regional

735   anthropogenic dust column burden (DCB) (and percent contribution by

736   region);regional dust column burden (DCB); and percent contribution to regional

737   DOD.

Region	Mean anthropogenic DOD	Area (km^2)	Anthropogenic DCB (Tg)	DCB (Tg)	Contribution to regional DOD (%)
Wet	0.12	1.77×10^7	2.48(41.2)	3.09	80.3
Semi-arid & semi-wet	0.07	2.46×10^7	3.16(52.5)	4.67	67.7
Arid	0.06	1.21×10^6	0.38(6.3)	0.56	67.9

738
739

740

741   Table 2. Description of dust study areas. Latitude and longitude ranges; area and

742   percent of the region considered to contribute to anthropogenic dust emissions; and

743   annual mean anthropogenic dust column burden (ADCB) of the regions considered in

744   this study.

Region	Longitude Range	Latitude Range	Anthropogenic area km^2(%)	Mean ADCB (g m^{-2})
Eastern China	100.0 °E-130.0 °E	25.0 °N-50.0 °N	3.71×10^{6}(63.0)	0.17
India	60.0 °E-90.0 °E	5.0 °N-27.5 °N	1.98×10^{6}(70.2)	0.42
North America	135.0 °W-65.0 °W	20.0 °N-50.0 °N	5.56×10^{6}(54.0)	0.09
North Africa	20.0 °W-35.0 °E	0.0 °N-30.0 °N	3.40×10^{6}(21.5)	0.26

745

746

747
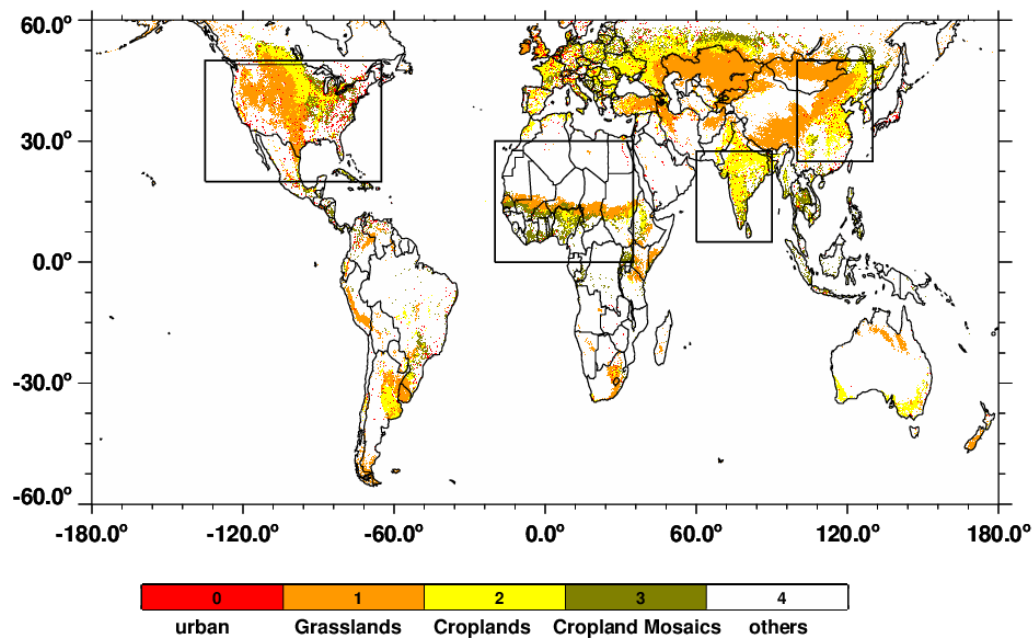
Fig. 1. Global distribution of the land cover types for anthropogenic dust source types (including urban, cropland and grasslands) retrieved by combing MODIS and GRUMP data. The black rectangles denote four majors source regions studied: Eastern China, India, North America, and Africa.

748
749
750
751
752
753

754
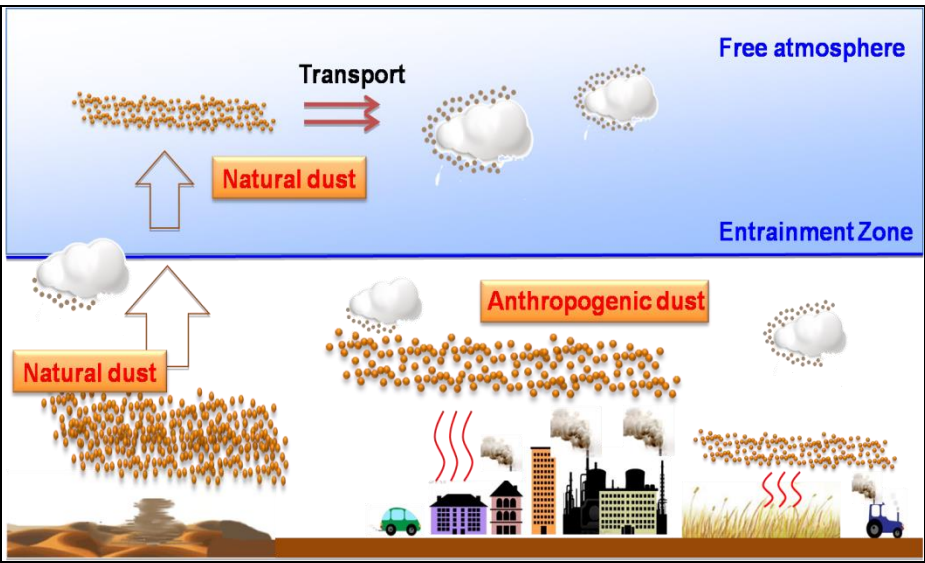
755

756

757 Fig. 2. A conceptual schematic for sources and transport of dusts upon which the
758 detection process of anthropogenic dust is based. The yellow dots represent dust
759 aerosol in the atmosphere; the arrow and red wavy lines represent lifting and
760 turbulence, respectively.

761

762

763

764
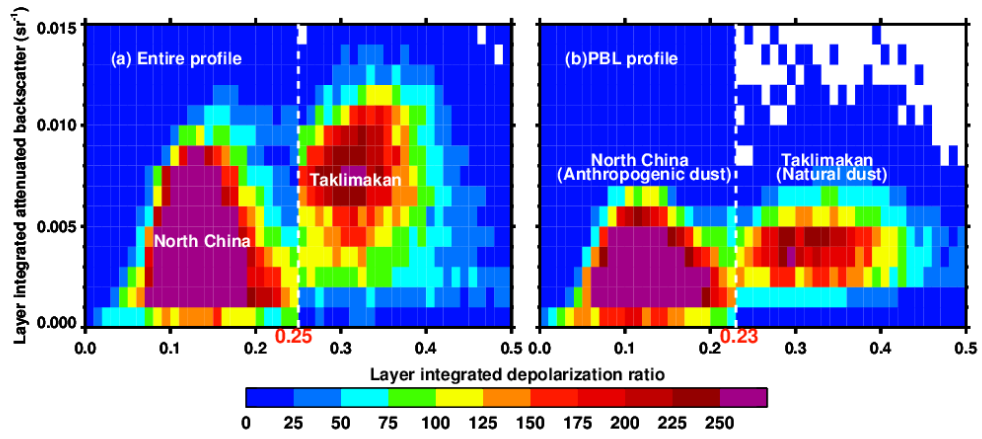
Fig. 3. The relationship between the layer-integrated depolarization ratio δ' and the layer-integrated attenuated backscatter coefficient γ′ for North China and Taklamakan from the entire profile (a) and within the PBL (b), respectively. The color of each pixel represents the frequency of occurrence for a $\Delta\delta'-\Delta\gamma'$ box measuring 0.01-by-0.001 sr^{-1}.

771

772
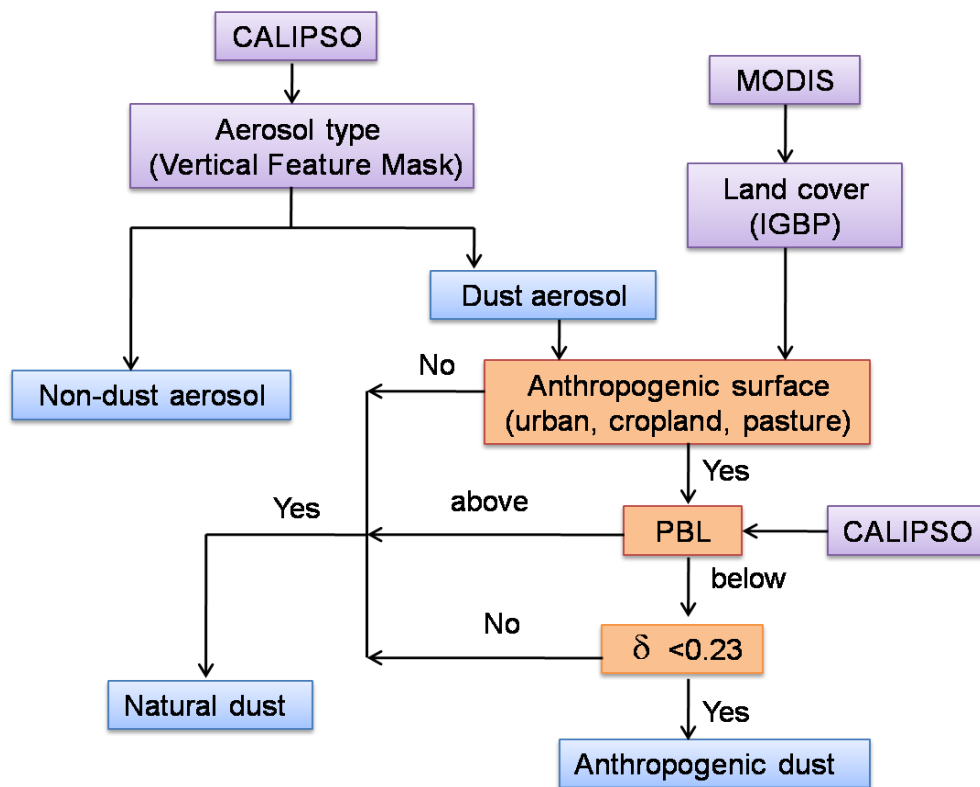
773

774 Fig. 4. Flow chart of anthropogenic dust detection by combing CALIPSO and land
775 cover dataset provided MODIS.

776

777

(a) Spring (MAM) **(b) Summer (JJA)**
(c) Autumn (SON) **(d) Winter (DJF)**

778
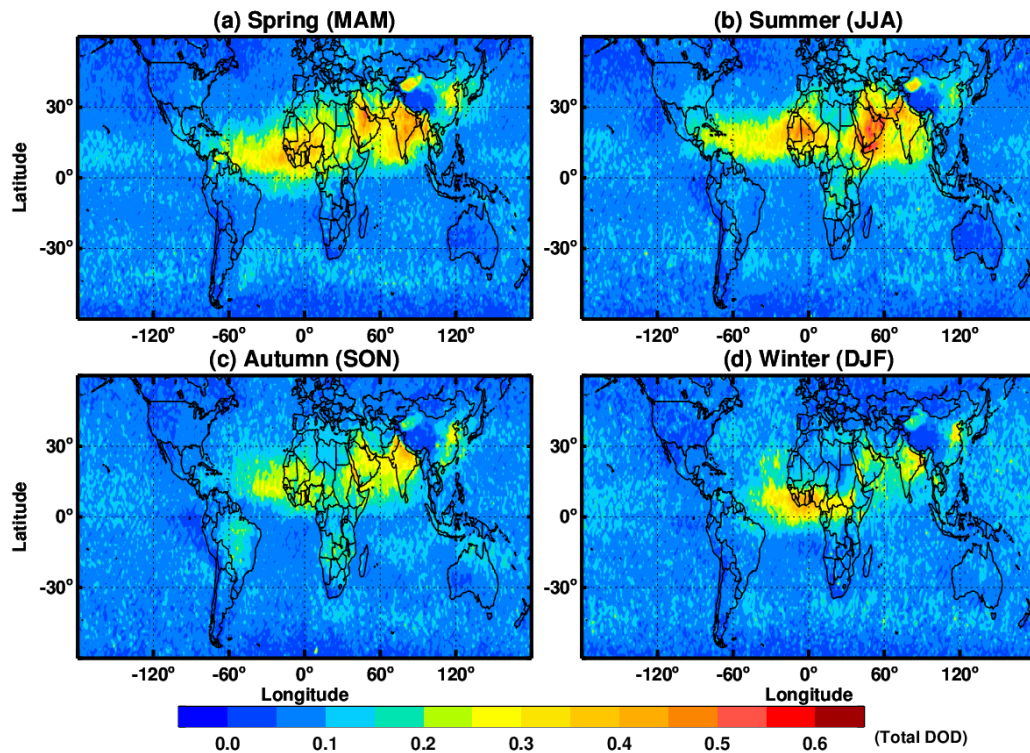
Fig. 5. Global distributions of seasonal mean for total dust optical depth derived from CALIPSO measurements from 2007 through 2010.
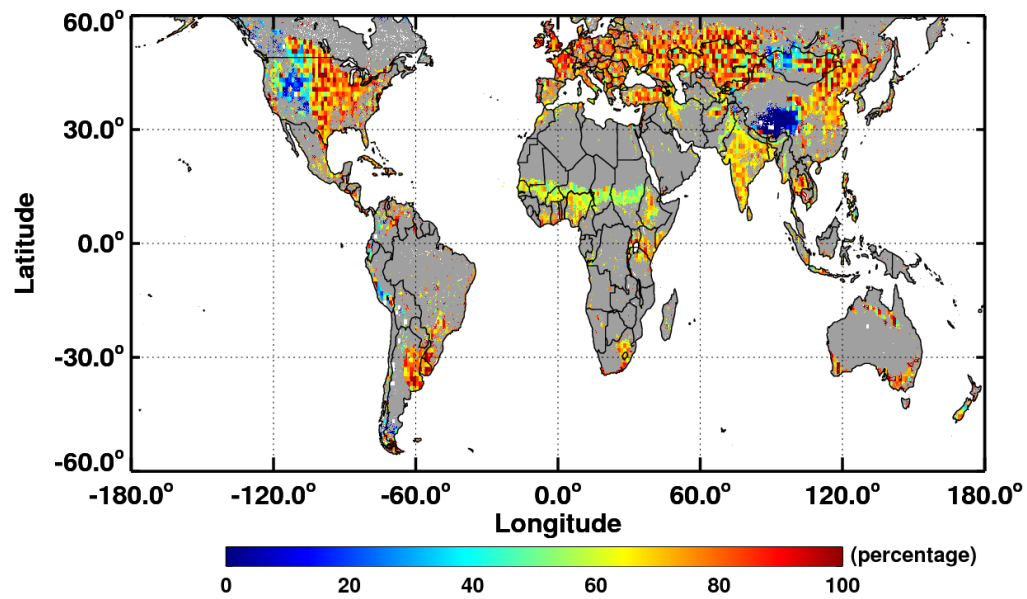
781

782

(a) Spring (MAM) (b) Summer (JJA)
(c) Autumn (SON) (d) Winter (DJF)
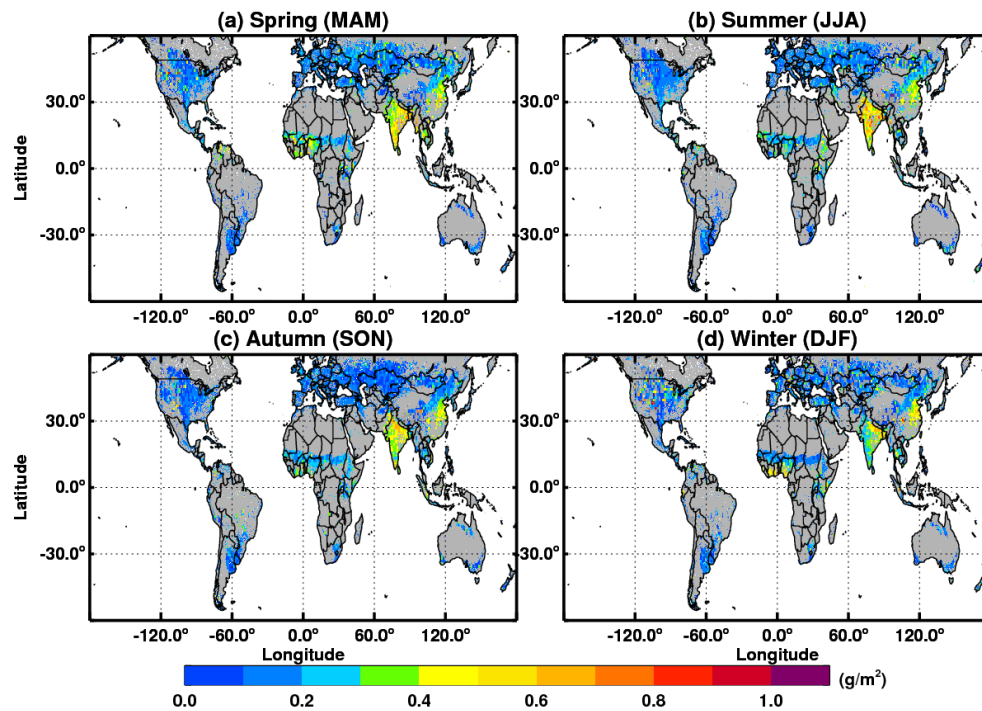
783
784 Fig. 6. Global distribution of seasonal mean for anthropogenic dust column burden
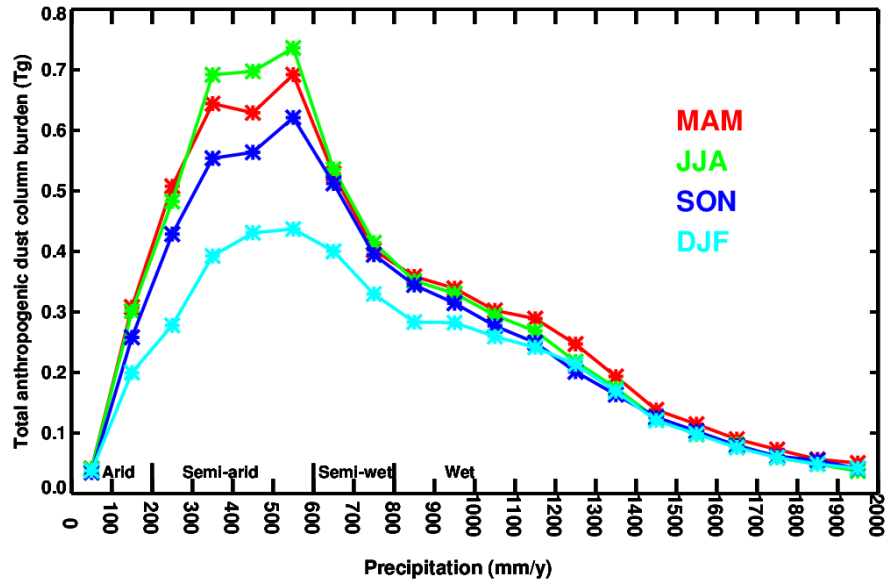785 from 2007 through 2010. The gray areas represent non-anthropogenic dust source
786 over land.
787
788

789

790
791 Fig. 7. Global distribution of the percentage of anthropogenic dust within the total
792 dust column burden.
793

Fig. 8. Comparisons of dust column burden over four seasons as a function of climatological mean precipitation. The precipitation interval is 100 mm yr^{-1}.
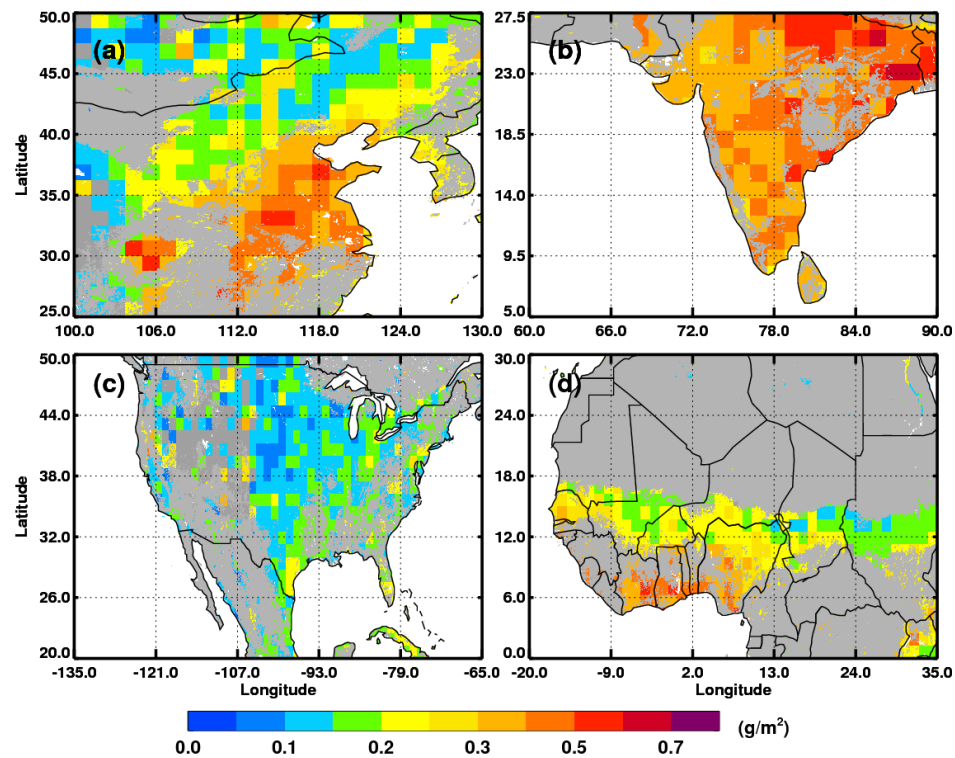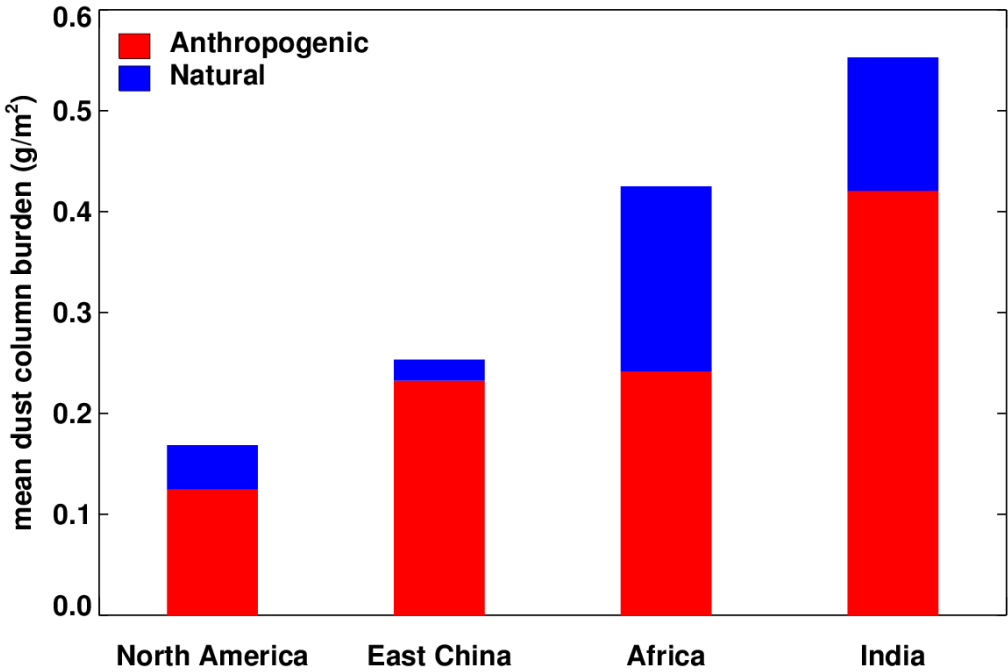
799

Fig. 9. Regional distribution of annual mean anthropogenic dust column burden derived from CALIPSO measurements (2007 through 2010) for a) Eastern China, b) India, c) North America, and d) North Africa.

805

806

807

808 Fig. 10. Comparison of the relative contribution of mean anthropogenic (red) and

809 natural (blue) dust column burdens in four geographical regions.

810

811